Acta Astronautica 160 (2019) 421–432

Contents lists available at ScienceDirect

Acta Astronautica

journal homepage: www.elsevier.com/locate/actaastro

# Concept of small satellite UV/visible imaging spectrometer optimized for tropospheric $NO_2$ measurements in air quality monitoring

Tamaki Fujinawa[a,e], Katsuyuki Noguchi[b], Akihiko Kuze[c], Andreas Richter[d], John P. Burrows[d], Andreas C. Meier[d], Tomohiro O. Sato[a], Takeshi Kuroda[a], Naohiro Yoshida[e], Yasko Kasai[a,e,*]

[a] National Institute of Information and Communications Technology, 4-2-1, Nukuikitamachi, Koganei, Tokyo, Japan
[b] Faculty of Science, Nara Women's University, Kitauoyanishimachi, Nara-city, Nara, Japan
[c] Japan Aerospace Exploration Agency, 2-1-1, Sengen, Tsukuba, Ibaraki, Japan
[d] Institute of Environmental Physics, University of Bremen, Bibliothekstraße 1, 28359, Bremen, Germany
[e] Environmental Chemistry and Engineering, Tokyo Institute of Technology, 4259, Nagatsuta-cho, Midori-ku, Yokohama, Kanagawa, Japan

ARTICLE INFO

*2010 MSC:*
00-01
99-00

*Keywords:*
Nitrogen dioxide
Earth observation
Radiative transfer model
Remote sensing

ABSTRACT

Satellite observations at nadir can potentially facilitate a better understanding of the emissions and distribution of tropospheric nitrogen dioxide, $NO_2$, which is a well-known pollutant. The identification of emissions requires adequate spatiotemporal resolution measurements of the total column amounts of $NO_2$. The spatial resolution of previous and current observations is insufficient for the identification of $NO_2$ hot-spots. Switching to a spatial resolution of ~ 1 km × ~ 1 km can improve the identification of local sources of $NO_2$ and their emissions. To investigate the feasibility of observations with such a high spatial resolution, we simulated radiance spectra for different cases under varying parameters, such as area, season, satellite altitude, and surface reflectance by using the radiative transfer model SCIATRAN. We subsequently retrieved $NO_2$ slant column densities (SCDs) using the differential optical absorption spectroscopy (DOAS) technique with several fit windows. For test cases associated with polluted conditions, we found that the conceptual nadir-observing instrument on a satellite at an altitude of ~ 300 km involved the lowest retrieval errors for signal-to-noise ratios of around 1000 with accuracy better than the required 5% for tropospheric $NO_2$ SCD and that the fit window of 425–497 nm met the scientific requirements for both surface reflectance cases.

## 1. Introduction

Nitrogen dioxide ($NO_2$) is one of the most important trace gases in the troposphere, participating in catalytic cycles that result in the production of ozone ($O_3$), and its oxidation to nitric acid, $HNO_3$, results in the acidification of aerosols. As is well known, the anthropogenic production of $NO_x$ (the sum of NO and $NO_2$) from fossil fuel combustion leads to smog and poor air quality episodes. This in turn affects human health, especially through the entry of aerosol particles of extremely small diameter (less than 2.5 μm) and $O_3$ into the cardiovascular system. $NO_2$ itself is also toxic. According to the World Health Organization (WHO), ambient outdoor air pollution is estimated to have caused 3 million premature deaths worldwide in 2012, in both cities and rural areas, especially in South–East Asia and the Western Pacific region [1]. The main sources of $NO_2$ are anthropogenic, especially fossil fuel combustion (e.g., power plants and vehicles) at urbanized sites. Since the Industrial Revolution, fossil fuel combustion has emerged as the major source of NO and $NO_2$ owing to the rapid increase in its use as a source of energy for domestic heating, power generation, industry, and transport. Over polluted regions, 50%–90% of the $NO_2$ exists in the troposphere depending on the degree of pollution, where it has a typical photochemical lifetime of several hours [2].

Global observations of tropospheric $NO_2$ from space, using instruments such as the Global Ozone Monitoring Experiment (GOME; [3]), the Scanning Imaging Absorption Spectrometer for Atmospheric Cartography (SCIAMACHY; [4]), the Ozone Monitoring Instrument (OMI; [5]), and GOME-2 [6], all operating on low earth orbit (LEO) satellites orbiting at an altitude of around 800 km, have provided us with a better understanding of the emissions, spatiotemporal distributions, and long term trends since the mid-1990s, on the basis of the differential optical absorption spectroscopy (DOAS) technique [7–17]. In addition, the Sentinel-5 Precursor (TROPOMI; TROPOspheric Monitoring Instrument), which was launched in October 2017 at an orbit of 824 km, began to observe atmospheric trace gases including $NO_2$ with a high

* Corresponding author. National Institute of Information and Communications Technology, 4-2-1, Nukuikitamachi, Koganei, Tokyo, Japan..
*E-mail address:* ykasai@nict.go.jp (Y. Kasai).

https://doi.org/10.1016/j.actaastro.2019.03.081
Received 8 November 2018; Received in revised form 20 March 2019; Accepted 28 March 2019
Available online 01 May 2019
0094-5765/ © 2019 IAA. Published by Elsevier Ltd. All rights reserved.

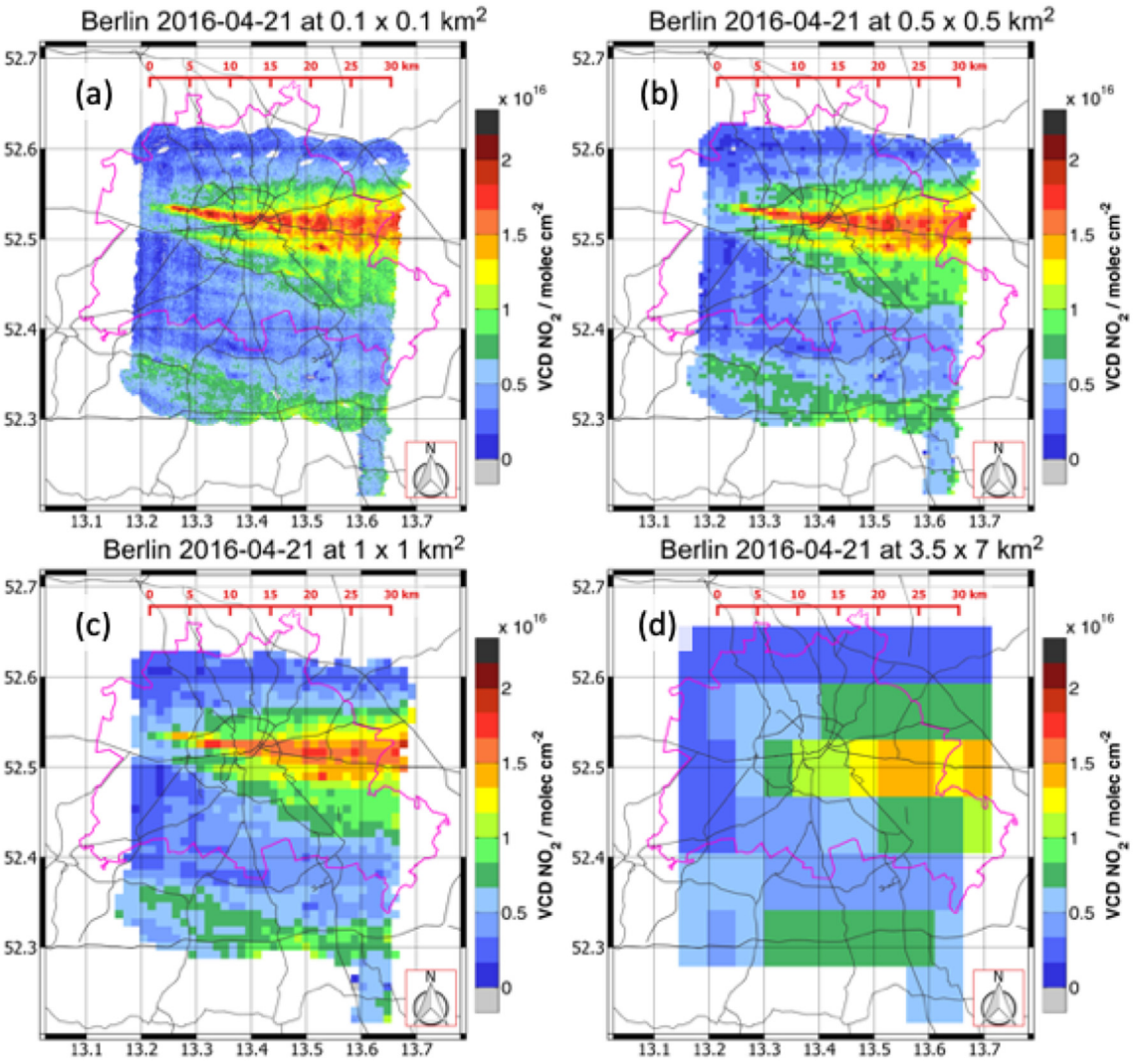


**Fig. 1.** $NO_2$ VCD measured by AirMAP in the morning (~ 07:30–09:30 UTC) of April 21, 2016, averaged to a horizontal resolution of **(a)** 0.1 × 0.1 km$^2$, **(b)** 0.5 × 0.5 km$^2$, **(c)** 1 × 1 km$^2$, and **(d)** 3.5 × 7 km$^2$.

spatial resolution of 3.5 × 7 km$^2$ [18]. As existing LEO instruments prioritize observations with global coverage rather than diurnal variations of atmospheric gas species, they use sun-synchronous orbits that pass the measurement location at a fixed local time. Satellite instruments in geostationary earth orbit (GEO), which are at an altitude of around 36000 km, enable us to conduct optimal temporal sampling of a specific region and obtain information on the diurnal variations. Furthermore, advanced air quality monitoring missions using a GEO satellite constellation, namely GEO-AQ, are being developed for launch in the 2018–2026 time frame, as are complementary LEO satellite missions, including Sentinel-5 (S5) on the MetOp-SG series, which is the successor to GOME-2 and has a better match with the spectral observations of SCIAMACHY, Ozone Mapping Profiler Suite (OMPS) [19] on the Suomi National Polar orbiting Partnership (Suomi-NPP) and Joint Polar Satellite System (JPSS), and Environment Monitoring Instrument (EMI) on the GaoFen-5 satellite. The GEO-AQ constellation comprises the Geostationary Environment Monitoring Spectrometer (GEMS, Korea) [20], Sentinel-4 (ESA) [18], and Tropospheric Emissions: Monitoring of Pollution (TEMPO, NASA) [21]. The nominal spatial resolution for observations is 2–8 km at the middle latitudes, which is extremely high compared to existing LEO satellites, e.g., 13 × 24 km$^2$ for OMI nadir. The GEO-AQ and potential LEO satellite missions (e.g., Spectrolite [22]), together with ship- or ground-based observations [23,24] and aircraft measurements [25], are expected to facilitate synergistic analyses for the study of air pollution.

Although the spatial resolution of the GEO-AQ and TROPOMI instruments is extremely high, it remains inadequate for maximizing the number of cloud-free observations and effectively separating large point sources that are clustered together in urban regions. To obtain the best information about local sources, an observation with a kilometer-order horizontal resolution, e.g., 1 × 1 km$^2$, is required. A spatial resolution of 1 × 1 km$^2$ enables us to detect local emission plumes of $NO_2$, although there is a trade-off between spatial resolution and observation frequency. Switching to a spatial resolution of 1 km coupled with global and adequate diurnal sampling by a future constellation would address issues such as understanding the turbulent mixing of emissions into the air mass and its effects on transport and transformation, as well as the short-term evolution of pollution plumes.

We investigated the observation capability and proposed the optimal setup for the observational wavelength domain, altitude of the satellite, and sensor specifications by performing simulations for $NO_2$ measurements under the assumption of a LEO satellite. The instrumental concept discussed in the present study is inherited from the SCIAMACHY project and studies for potential Japanese air quality monitoring missions, such as Air POLLution Observation (APOLLO), Geostationary mission for Meteorology and Air pollution (GMAP-Asia) [26,27], the SCIA-ISS concept, and the uvSCOPE mission, which have been candidates for the Earth observation section of the International

Space Station (ISS). Our objectives for the instrument considered in this study are as follows: (i) to observe the entire globe with a high spatial resolution of 1 × 1 $km^2$; and (ii) to specialize in $NO_2$ observations using an optimal fit window for $NO_2$ retrieval. To test the feasibility of such an instrument, we estimated the signal-to-noise ratios (SNRs) of the proposed sensor and the measurement errors of the tropospheric $NO_2$ slant column densities (SCDs) with a horizontal resolution of 1 × 1 $km^2$.

The remainder of this paper is organized as follows. Section 2 describes the setup used in the sensitivity study, i.e., the setup for the radiative transfer calculation, the setup for the given sensor specification and derivation of the SNR of the sensor, and the setup for the error analysis method. Section 3 discusses the observation capability on the basis of comparison results of measurement errors of the retrieved $NO_2$ SCDs for each geometry and the relationships between the SNRs and the measurement errors. The final section summarizes our findings and concludes the paper.

## 2. Setup for the sensitivity study

To determine the optimal space-based resolution for the estimation of $NO_x$ emissions using the total tropospheric $NO_2$ column amount from urban sources, we adopt a pragmatic approach. This is because the size of $NO_2$ plumes depends on several factors, namely the size and distribution of urban sources, the wind speed and direction, the processes that mix the air from the source into the wind flow, which are in part turbulent, etc. Consequently, to determine the optimal spatial resolution, we used $NO_2$ observations from aircraft remote sensing measurements obtained by the University of Bremen instrument, namely AirMAP [25,28]. AirMAP was flown on an FU-Berlin Cessna aircraft in a variety of campaigns to investigate $NO_2$ plumes from urban sources, power plants, and shipping [25,29,30].

As an example, Fig. 1 shows the $NO_2$ VCD below the aircraft, measured by AirMAP in the morning (~ 07:30–09:30 UTC) of April 21, 2016, i.e., a weekday (Thursday), above the city of Berlin. The city borders and major roads are shown by pink and black lines, respectively. Flights were performed within the AROMAPEX campaign with the objective of comparing airborne imaging DOAS instruments [31]. Details of the instrument and the analysis of the data shown here can be found in Ref. [32]. The wind conditions on this day were close to a good approximation constant during the 2 h required to obtain the aircraft measurements.

Fig. 1 shows the $NO_2$ VCD data averaged to **(a)** 0.1 km × 0.1 km, **(b)** 0.5 km × 0.5 km, **(c)** 1 km × 1 km, and **(d)** the nominal TROPOMI resolution of 3.5 km × 7 km. As can be seen, the two large but different urban plumes are readily discerned in panels **(a)–(c)** but not in panel **(d)**. We note that winds are generally relatively strong at the middle latitudes compared to the sub-tropical and tropical latitudes. Even the much improved spatial resolution of the highest currently available space-based remote sensing data will thus not be able to separate patterns such as those observed in Berlin. Therefore, we pragmatically conclude that a spatial resolution of ~ 1 km × ~ 1 km is required to effectively identify and separate such urban emissions sources.

In general, the instantaneous field of view (IFOV) of an instrument determines the spatial resolution of its measurement; thus, a low IFOV leads to a higher spatial resolution. However, a low IFOV degrades the SNR, as IFOV and SNR are trade-off parameters. The optical throughput, or etendue, which is related to SNR, is limited by the IFOV. Therefore, a super-low-altitude satellite is expected to be an important breakthrough for improving the spatial resolution of air quality monitoring, because it is easy to manage the trade-off parameters at low altitudes. In 2017, the Super Low Altitude Test Satellite (SLATS) was successfully launched by the Japan Aerospace Exploration Agency (JAXA) for use as a next-generation Earth observation satellite, at an orbit height of around 200 km, which provides a high spatial resolution and greater cost reduction in terms of compact and lightweight satellite sensors and launch services [33,34]. Satellite stability is challenging at low altitudes (less than 300 km), where the air drag is 1000 times greater than that at 600 km. After the demonstration, the stabilization technique could contribute a satellite constellation at a super-low altitude to facilitate frequent and global observations for chemical weather forecasting, hazard management, and emission source identification over short and long time scales. In this study, we considered a satellite altitude of 300 km in addition to 600 km.

We performed simulations for various cases to derive SNRs for the given satellite instrument and to calculate the measurement errors of tropospheric $NO_2$ SCDs ($\varepsilon$) using the radiative transfer model (RTM) SCIATRAN, which has been developed to calculate atmospheric radiance spectra in any observation geometry [35], as well as the DOAS method. The analytical method used in this simulation is based on previous studies [36–38]. The method comprises three parts: the RTM calculation setup, the instrumentation setup and SNR calculation, and the DOAS retrieval method. The RTM calculation setup and DOAS retrieval method are described in detail in Sections 2.1 and 2.3, respectively. Section 2.2 describes the given instrumentation setup and the SNR derivation.

In this study, we determined the scientifically required measurement error to be 5% (corresponding to around 3 × $10^{15}$ molec. $cm^{-2}$ tropospheric $NO_2$ VCD under polluted conditions) on the basis of results obtained in previous investigations for a representative area of interest (Beijing) [39,40]. Ma et al. [39] reported that the daily mean values of the $NO_2$ tropospheric VCDs in the Beijing area, which is the most heavily polluted city in East Asia, ranged from 0.2 to 16.8 with an average of 5.8 in winter, and 0.5 to 13.3 with an average of 3.6 in summer from 2008 to 2011, in units of $10^{16}$ molec. $cm^{-2}$. Therefore, we assumed that a scientific requirement of less than 5% would be sufficient to detect $NO_2$ hot-spots and to identify individual sources, although it should be noted that satellite observations over this site had negative biases of up to 50% because of the $NO_2$ horizontal gradients, the assumed profile shape of $NO_2$, and aerosols, as well as systematic differences between the two observational bases [39,41]. For comparison, we also considered an unpolluted site (Hokkaido) in the present study. In addition, we simultaneously considered several realistic parameters related to the $NO_2$ observations.

### 2.1. Radiative transfer calculation setup

We simulated Earth's backscattered radiance spectra for several cases using SCIATRAN to obtain realistic radiance spectra by considering three different parameters, namely geometry, profile shape, and surface reflectance. To ensure that our parameters were realistic, parameters such as area, season, satellite altitude, and fit window were specifically assigned as stated in Table 1. In addition, we simulated radiance spectra using a vertical profile of tropospheric $NO_2$ concentration of nearly zero for each geometry case in order to calculate the stratospheric (from the tropopause up to the top of the atmosphere) contribution of $NO_2$ in the subsequent analysis. We used the incident

**Table 1**
Parameter setup used in this simulation.

| Parameters | Characteristics |
|---|---|
| Instrument | |
| Wavelength range | 425–450 nm<br>425–497 nm<br>405–465 nm |
| Satellite altitude | 300 km (IFOV = 0.19 °)<br>600 km (IFOV = 0.1 °) |
| Situation | |
| Area | Beijing (40.5 °N, 115.3 °E)<br>Hokkaido (43.3 °N, 143.4 °E) |
| Season | Winter (January 2010)<br>Summer (July 2010) |

solar irradiance spectrum obtained from the data of Chance and Kurucz [42]. The RTM calculation was performed using the discrete ordinate method from 401.0 to 500.0 nm in wavelength steps of 0.01 nm under cloud-free conditions in order to avoid complicating the RTM calculation. The modeled atmosphere was set to 0–100 km with a vertical resolution of 200 m for altitudes of 0–10 km, 500 m for 10–12 km, and 1 km for 12–100 km. The radiance spectra calculated by SCIATRAN were convolved with a Gaussian slit function with a full width at half maximum (FWHM) of 0.2–0.5 nm (depending on the fit window). In addition, we considered aerosol effects for all cases in the RTM calculations. A detailed description of the aerosol effects is provided in Section 2.1.4.

#### 2.1.1. Geometry

We considered the Beijing and Hokkaido (the northernmost prefecture of Japan) areas as examples of polluted and unpolluted regions, respectively. This is because Beijing is one of the most urbanized cities in East Asia and is thus a suitable representative polluted region [9,41]. By contrast, the Hokkaido area is relatively clean and latitudinally similar to Beijing; thus, it is a suitable candidate for comparison. In addition, we considered two seasons, winter (January) and summer (July), for both areas in order to consider different solar zenith angles (SZAs) and vertical profiles. We assumed that the satellite instrument was in a sun-synchronous orbit and orbiting at an altitude of 300 km or 600 km while looking at the nadir in each case. In other words, the satellite position was set to be constantly located at the zenith through the RTM calculation. Therefore, the relative azimuth angle (the angle between the sun and the satellite at the ground surface) and line-of-sight viewing angle were set to zero for each case. The SZA was set to the monthly mean value for each area and season as defined in Table 1 by assuming that the descending node is at 10:30 LT. Furthermore, we assumed that the observing swath width was as narrow as 200 km; thus, the effects of off-nadir measurements on the light path and the spatial resolution were negligible in this simulation.

#### 2.1.2. Profile shape

Fig. 2 shows the vertical profiles of trace gases as well as the pressure and temperature used in this simulation. We employed monthly mean results in the Beijing and Hokkaido areas from the CHASER model [43] for the tropospheric vertical profiles of $NO_2$, $SO_2$, $O_3$, BrO, and HCHO in 2010, when there was a rapid increase in $NO_x$ emissions in China [44]. The CHASER model has been well evaluated [45] and validated through comparisons with the MAX-DOAS $NO_2$ measurements [41]. The vertical profile data were calculated with a horizontal spatial resolution of T42 (2.8 ° × 2.8 °) and 32 vertical layers from the surface up to about 3 hPa altitude. Subsequently, the profiles were directly combined with the annual mean values of the SOCRATES model [46], which is a two-dimensional global chemistry climate model of Earth's atmosphere, from the tropopause up to 100 km, with the same profile shape for all cases. The (thermal) tropopause altitudes were determined by the lapse rate derived from the temperature profiles of the CHASER results on the basis of the WMO 1985 definition. Finally, the vertical profiles were linearly interpolated to the grid used in SCIATRAN. As shown in Fig. 2, the $NO_2$ levels in the Beijing area (red thick line) were at most ten times higher from the surface to around 2 km compared to those in the Hokkaido area.

#### 2.1.3. Surface reflectance (albedo)

Fig. 3 shows the distribution of the monthly mean values of OMI/Aura Surface Reflectance Climatology Level 3 Global 0.5deg Lat/Lon Grid data (OMLER) [47] for the period 2005–2009 in January (upper) and July (lower). Similar surface reflectance and the seasonal trend between Beijing and Hokkaido can be seen in the rectangular region surrounded by broken lines, which represents the grid of the CHASER model. As shown in Fig. 4, the monthly mean values of surface reflectance data extracted in the above-mentioned grid ranged from around 0.05 to 0.08 with a negative peak in summer in Beijing (red line), whereas in Hokkaido (blue line), they ranged from 0.04 to 0.07 with the same trend but were smaller by 0.01 compared to those in Beijing except in August. On the basis of these data, we employed 0.05 and 0.1 as the typical values of surface albedo in both Beijing and Hokkaido in summer and winter, respectively. Lambertian surface reflectance was assumed in the RTM calculations.

#### 2.1.4. Aerosol

We considered aerosols in the RTM calculations to simulate a realistic atmosphere. Scattering or absorption by aerosols influences the $NO_2$ VCD calculation through the air mass factor (AMF) term [14,48]. Typical aerosol scenarios were considered for each area and season on the basis of mixing states described by Hess et al. [49] (see Table A.1, Appendix A). The vertical profiles of the aerosol extinction coefficients used in RTM calculations are shown in Fig. 5. The aerosol extinction coefficient profiles decreased exponentially with height, with a scale height of 3 km from the surface to 2 km, 8 km from 2 km to 10 km, and 99 km from 10 km to 100 km. The detailed aerosol scenarios are summarized in Table A.1.

### 2.2. Instrumental setup and the SNR calculation

In this study, we consider a new satellite instrument employing a two-dimensional CMOS array sensor and a compact, robust, and cost-effective optical system with aberration-corrected convex gratings, suitable for use in a satellite constellation for global air quality monitoring. The grating imaging spectrometer employed in this study was based on the spectrometer described by Kuze et al. [50,51], covering a wide swath without a moving mechanism on the basis of satellite motion to observe the entire globe. The spectrometer can easily employ a custom-designed grating and foreoptics. As mentioned above, IFOV and SNR are trade-off parameters, and they can be tuned by small foreoptics. The satellite instrument concept used in this study has two major features: one is a high spatial resolution of $1 \times 1\ km^2$, and the other is a compact optical system covering a spectral window optimized for $NO_2$ retrieval.

Irie et al. [36] performed sensitivity studies for the instrumentation concepts of GMAP-Asia and quantitatively showed the relationship between measurement precision and sensor specifications. Following the analytical method proposed by Irie et al. [36], Noguchi et al. [38] demonstrated that the diurnal variation of tropospheric $NO_2$ over Tokyo can be detected by the GMAP-Asia UV/visible sensor with a FWHM of 0.4 nm and a sampling ratio of 4 (number of pixels per FWHM) at SNR > 500. Noguchi et al. [52] also investigated the effect of surface reflectance anisotropy on tropospheric $NO_2$ measurements assuming the GMAP-Asia UV/visible sensor specifications. The present study focused not on a GEO satellite instrument but on a LEO satellite instrument.

We introduced the following assumptions about the instrument and its performance to simulate the realistic SNR of the detector:

- a two-dimensional Si–based CMOS array sensor with a size of $13 \times 13\ mm^2$ was assumed for an individual detector,
- the size of one pixel was assumed to be $6.5\ \mu m$ and 3 pixels were binned resulting in a sampling ratio of 2.5–5 pixels per FWHM,
- an empirical detectivity considering the degradation due to the array and read out electronics was introduced and assumed to be $2.0 \times 10^{13}\ cm\ Hz^{1/2}\ W^{-1}$,
- the optical efficiency including the quantum efficiency was assumed to be 0.43.

Neither the optical efficiency nor the quantum efficiency of the detector can be accurately quantified in advance; hence, the systematic errors related to the instrument were not considered in this study, although the optical parameters summarized in Table 2 are realistic on

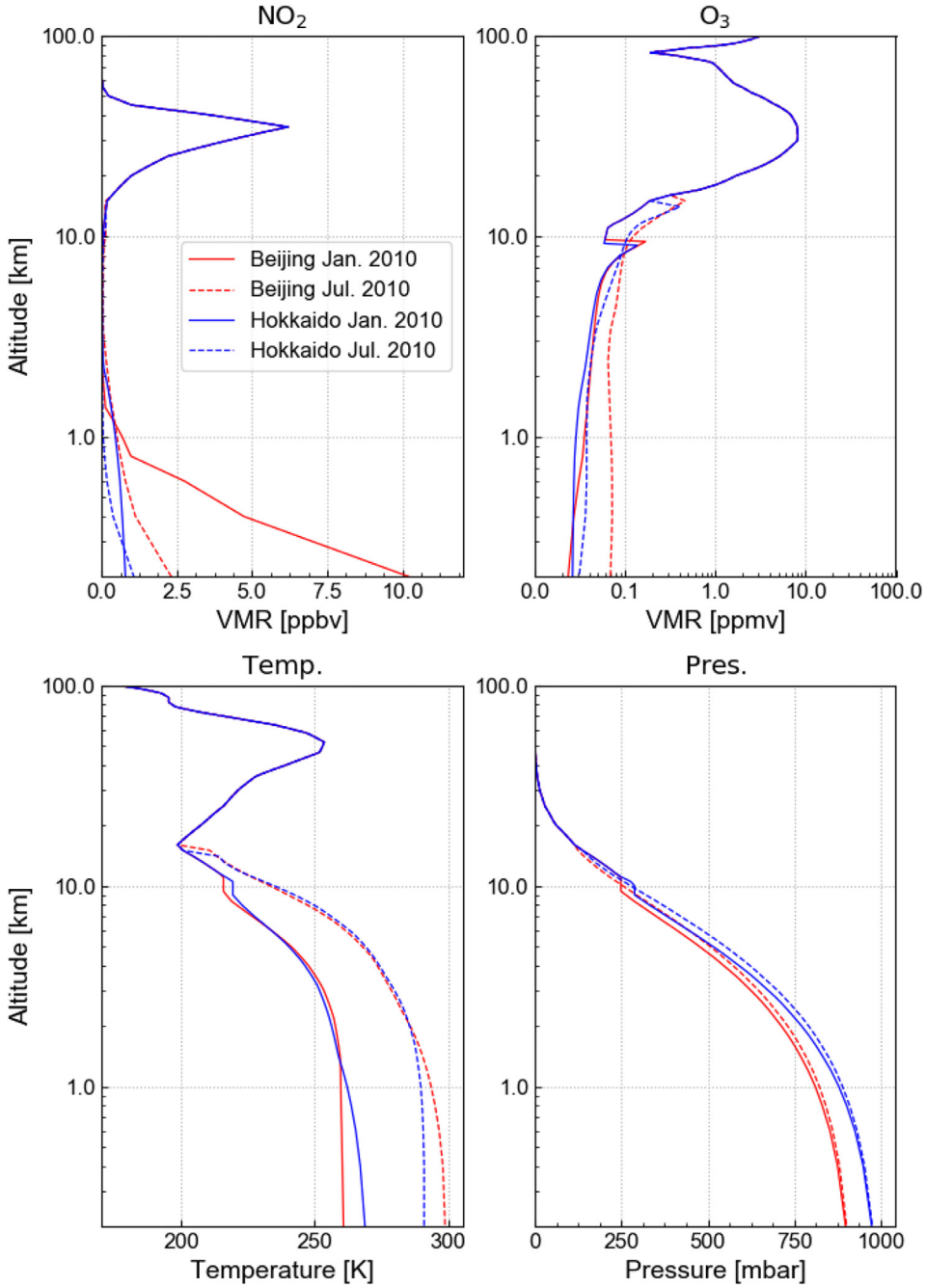


**Fig. 2.** Vertical profiles of $NO_2$, ozone, pressure, and temperature used in SCIATRAN for each area and season.

the basis of nominal proposed specifications.

We considered two types of SNRs. One is a constant SNR (500, 2000, 5000, and 10000), and the other is a more realistic type that depends on the sensor specifications and is defined as follows:

$$SNR_{det} = \frac{D^* L A_c \Omega \Delta\nu \eta}{A_d^{1/2} \Delta f^{1/2}} \quad (1)$$

$$SNR_{total} = \frac{1}{\sqrt{\left(\frac{1}{SNR_{det}}\right)^2 + \left(\frac{1}{SNR_{sn}}\right)^2 + \left(\frac{1}{SNR_{dc}}\right)^2}} \quad (2)$$

where $D^*$: detectivity [cm $Hz^{1/2}$ $W^{-1}$], $L$: luminance measured by the detector [W $m^{-2}$ $str^{-1}$ $\mu m^{-1}$], $A_c$: optical system area [$m^2$], $\Omega$: targeting solid angle [str], $\Delta\nu$: spectral resolution [nm], $\eta$: optical efficiency [−], $A_d$: detector area [$m^2$], $\Delta f$: frequency [$s^{-1}$], $SNR_{sn}$: SNR of the shot noise, and $SNR_{dc}$: SNR of the dark current.

$SNR_{det}$ in Eq. (2) represents the SNR of the read noise of the detector. $D^*$ is a plausible detectivity value as described previously. The term $A_c \times \Omega$ represents the etendue of the optical system. The SNRs of the shot noise and dark current of the CMOS detector are represented as $SNR_{sn}$ and $SNR_{dc}$, respectively, and defined as follows: $SNR_{sn} = \sqrt{(L A_c \Omega \Delta\nu \eta \Delta t)\cdot\lambda/hc}$, $SNR_{dc} = SNR_{sn}\sqrt{\Delta t\, dc}$, where $\Delta t$ denotes the integration time in seconds and $dc$ dark current [e $pixel^{-1}$ $s^{-1}$] (= 120), respectively. The parameters used in the equations are listed in Table 2. In the following section, $SNR_{total}$ is simply referred to as SNR without a subscript.

### 2.3. DOAS retrieval

Corresponding to the above-mentioned SNRs, 1000 different

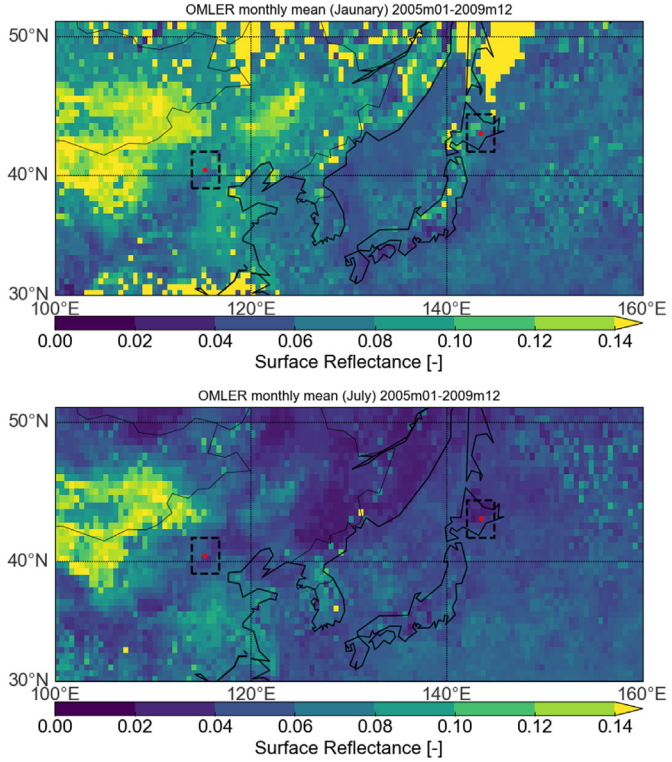


**Fig. 3.** Monthly mean maps of surface reflectance taken from OMI/Aura Surface Reflectance Climatology L3 Global Grid data for (**top**) January and (**bottom**) July. The data were obtained from January 2005 to December 2009. The red circles in both panels represent the Beijing and Hokkaido areas, and the rectangles with broken lines represent the grids of the CHASER model. (For interpretation of the references to color in this figure legend, the reader is referred to the Web version of this article.)

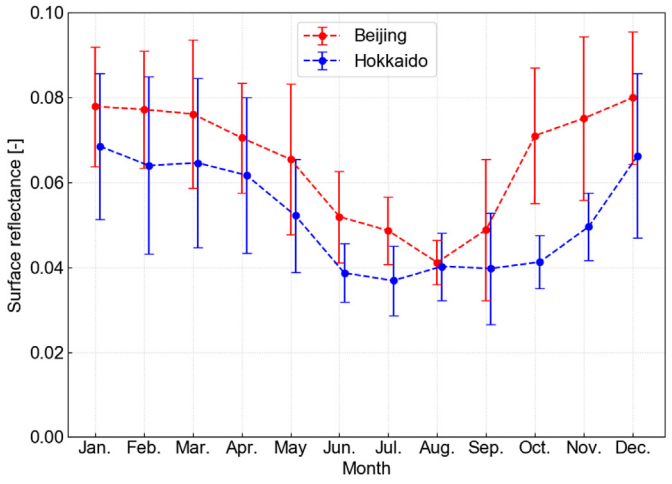


**Fig. 4.** Seasonal trend of the OMLER surface reflectance data in the same period as Fig. 3. The circles represent the mean values of the surface reflectance for the Beijing and Hokkaido areas, and the bars represent the one-sigma standard deviations for each month.

patterns of random noise were added to one radiance spectrum convolved with a slit function. We obtained 1000 spectra for each case of areas, seasons, satellite altitudes, and surface albedo values. We derived $NO_2$ SCDs from these spectra using the DOAS method [53]. The DOAS method is a well-established method for retrieving amounts of trace gases having spectral absorption features in the UV/visible range; it has been adopted in previous studies [3,4]. The DOAS is based on Beer-Lambert law and describes the attenuation of scattered sunlight passing

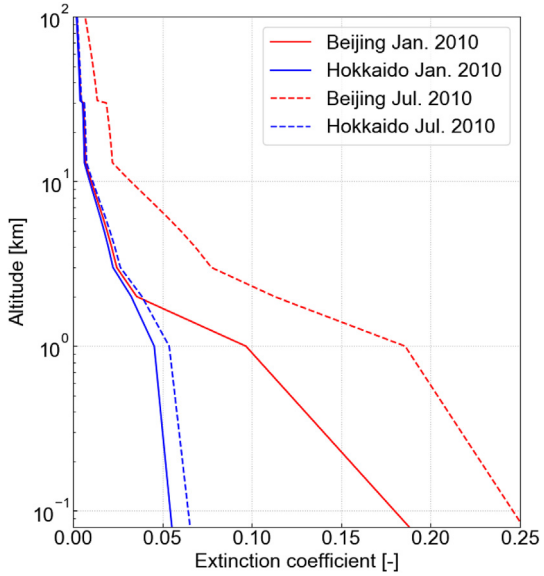


**Fig. 5.** Vertical profiles of aerosol extinction coefficients for each area and season.

**Table 2**
Characteristics of the optical system assumed in the present study.

| Parameters | Characteristics |
|---|---|
| Detector size | 0.065 mm |
| Aperture size | 0.74 cm |
| Read noise | 10 e |
| Dark current | 120 e/pixel/s |
| Detector aspect ratio | 1.0 |
| Effective detector area | 0.9 |
| Optical efficiency | 0.43 |
| Slit width | 0.065 mm |
| Time constant | 0.14 s |

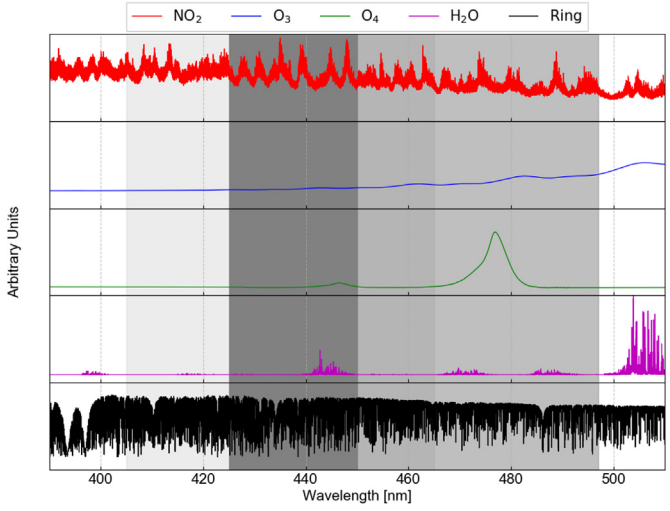


**Fig. 6.** Absorption cross-sections of trace gases used in DOAS retrieval. The shaded areas represent each fit window; 425–450 nm (dark gray), 425–497 nm (gray), and 405–465 nm (light gray). The absorption cross-sections for $NO_2$ (220 K), $O_3$ (223 K), $O_4$ (293 K), $H_2O$, and the Ring spectrum were obtained from the work of Vandaele et al. [57], Serdyuchenko et al. [58], Thalman and Volkamer [59], Rothman et al. [60], and Vountas et al. [61], respectively.

through the atmosphere. The spectral attenuation is separated into a high frequency part consisting of trace gas absorption structures and a low frequency part accounting for elastic scattering (Rayleigh and Mie scattering) which is approximated by a low order polynomial. In addition, the effects of inelastic rotational Raman scattering in combination with the highly structured solar spectrum, known as the Ring effect [54], is accounted for by a pseudo cross section as illustrated in Fig. 6 (black line). In DOAS, the optical depth ($\tau$), which is the natural logarithm of the ratio of the reference spectrum ($I_0$) to the measured spectrum ($I$), or $\ln(I_0/I)$, is described as a linear equation for each measurement wavelength ($\lambda$) with $SCD_i$ of $i$ absorbers and a closure polynomial of degree $p$ assuming that the logarithm of the scattering,

$$\tau = \ln\left(\frac{I_0(\lambda)}{I(\lambda)}\right) = \sum_i \sigma_i SCD_i + \sum_p c_p \lambda^p \quad (3)$$

We used three different well-validated wavelength domains for the DOAS fitting, i.e., 425–450 nm, 425–497 nm, and 405–465 nm, in order to investigate the optimal fit window for $NO_2$ retrieval, as our instrument is specialized for $NO_2$ observations. The wavelength range of 425–450 nm is a basic fit window that is frequently used for $NO_2$ retrieval, e.g., GOME measurements [7]. The improved fit window of 405–465 nm has been used for OMI measurements [55], while the wavelength range of 425–497 nm has been used for improved GOME-2 $NO_2$ retrieval by Richter et al. [56]. To exclude large-scale wavelength trends that include the effects of aerosols and other factors, a third-degree polynomial was used in the DOAS fitting. The absorption cross-sections for trace gases ($NO_2$, $O_3$, $H_2O$, $O_4$) and the Ring effect used in the DOAS fitting are shown in Fig. 6.

The total $NO_2$ SCDs were separated into tropospheric and stratospheric contributions by subtracting the stratospheric $NO_2$ SCDs from the total SCDs in order to determine the tropospheric $NO_2$ SCDs. We used a method similar to the reference sector method [7,62,63] to derive the tropospheric $NO_2$ contribution. This method regards the total $NO_2$ SCD over unpolluted regions (e.g., Pacific ocean) as the stratospheric $NO_2$ SCD through RTM calculations for each geometry. We used the results of the CHASER model in the Pacific region (180 °E), where the contribution of the tropospheric $NO_2$ to the total $NO_2$ SCD is small. Finally, we calculated the mean values and one-sigma standard deviations of the tropospheric $NO_2$ SCD distribution fitted with a Gaussian shape to estimate $\varepsilon$ of the $NO_2$ observations for each case.

## 3. Observation performance and capability studies

### 3.1. Determination of feasibility

Our target measurement precision is better than 5% (corresponding to $3.0 \times 10^{15}$ molec. $cm^{-2}$ in a highly polluted area) for a tropospheric $NO_2$ VCD. This corresponds to a tropospheric $NO_2$ SCD of around $3.0 \times 10^{15}$ molec. $cm^{-2}$ or less when using a tropospheric air mass factor (box air mass factor; b-AMF) of around 1 in the polluted region. This is based on the following general equation:

$$AMF = \frac{SCD}{VCD} \quad (4)$$

Fig. 7 shows the b-AMF for each layer, calculated by SCIATRAN for each region (polluted and unpolluted), and albedo (0.05 and 0.1) in winter and summer 2010, which depends on the a priori assumed profile shape and surface albedo. The b-AMF values were mostly less than 1 from the surface to 1 km and less than 3 from 1 km to the tropopause for the wavelength domain in both seasons, indicating that the tropospheric b-AMF was as small as 1 or less owing to the presence of aerosols, although the b-AMF above 10 km was nearly always greater than 3. With a surface albedo of 0.1, the b-AMF values at longer wavelengths were higher than those at shorter ones from the surface to the tropopause in both polluted and unpolluted regions.

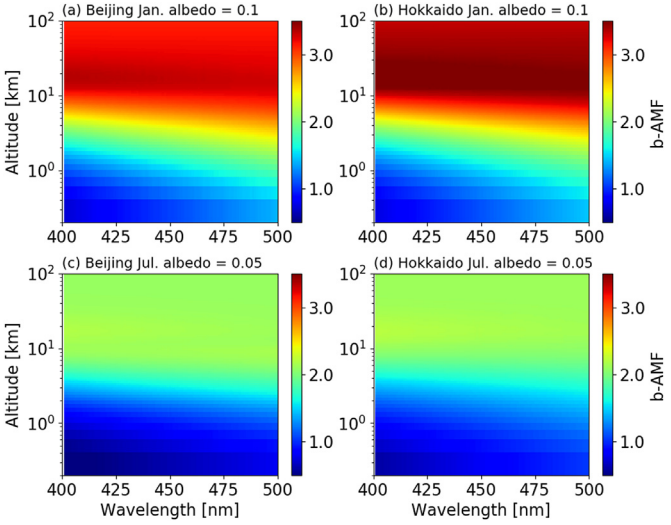


**Fig. 7.** Box air mass factor (b-AMF) calculated by SCIATRAN for January and July 2010 for polluted (**a,c**) and unpolluted (**b,d**) regions.

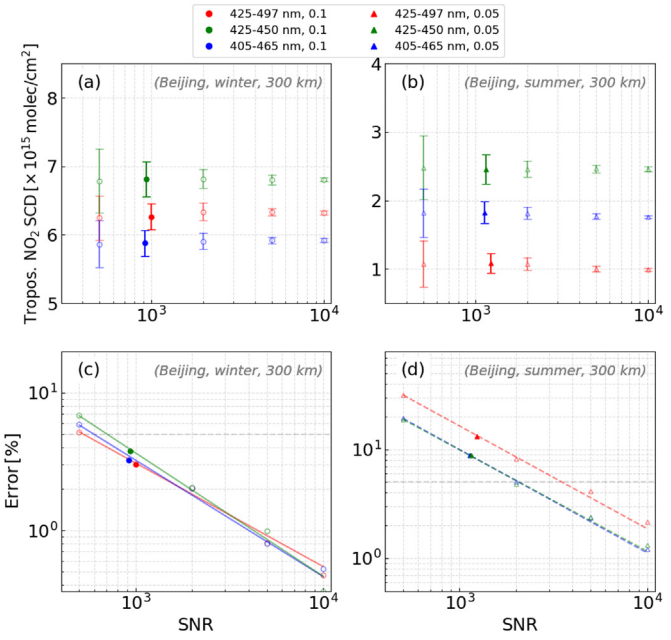


**Fig. 8.** Tropospheric $NO_2$ SCDs [$\times 10^{15}$ molec. $cm^{-2}$] and relative error [%] calculated for (**a,c**) Beijing in winter with albedo of 0.1 and (**b,d**) Beijing in summer with albedo of 0.05 at a satellite altitude of 300 km. The different colors represent the different fit windows. Note that the y-axes in each panel have different scales and those in the lower ones have logarithmic scales. The different symbols represent different albedo values (i.e., different seasons). The solid symbols represent SNR calculated at 450 nm using the given sensor specifications, while the open symbols represent a series of constant SNRs (i.e., 500, 2000, 5000, and 10000). The error bars in the upper panels represent one-sigma standard deviations of $NO_2$ SCDs calculated for each SNR. The horizontal broken lines in the lower panels represent the measurement requirements of 5% $NO_2$ slant column uncertainty. (For interpretation of the references to color in this figure legend, the reader is referred to the Web version of this article.)

#### 3.1.1. Comparison between different geometries

We calculated the SNRs for the given sensor specifications and then retrieved the tropospheric $NO_2$ SCDs using the DOAS for each considered case. Figs. 8 and 9 show the retrieved tropospheric $NO_2$ SCDs and the relative errors calculated in the two seasons for each SNR in the Beijing and Hokkaido areas, respectively. Each SNR represented by a solid circle was calculated at 450 nm for the given sensor specification

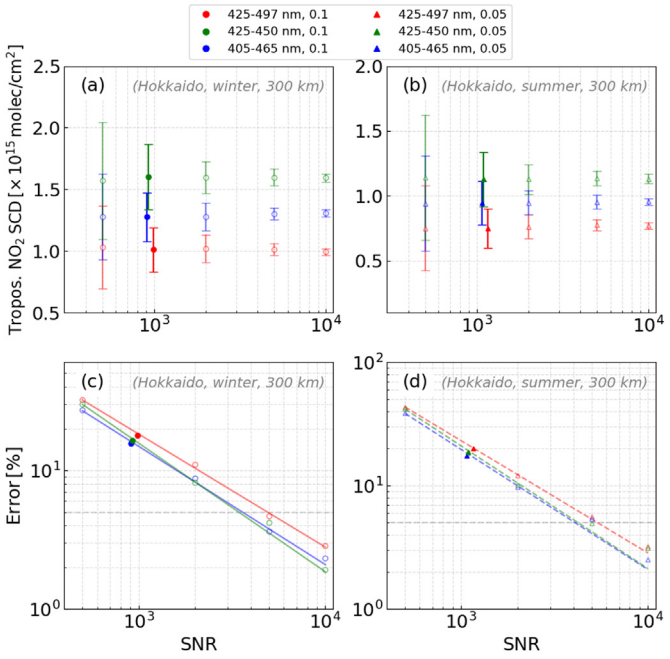


**Fig. 9.** Same as Fig. 8 but for Hokkaido.

using different fit windows, while the SNRs represented by open circles were a series of constant SNRs (i.e., 500, 2000, 5000, and 10000). The results using 425–497 nm showed the highest SNRs of around 1000 in winter and around 1300 in summer in both areas, while the results using 405–465 nm showed the lowest SNRs. They depend on different seasons, or SZAs, although they are comparable in both areas during the same season. It is interesting that in the case of enhanced $NO_2$ existing at the surface level (Fig. 8**(a)**), the tropospheric $NO_2$ SCD retrieved using 405–465 nm shows the lowest value ($5.9 \times 10^{15}$ molec. $cm^{-2}$ at SNR = 920), although in the other cases of lower surface $NO_2$ levels (Fig. 8**(b)**), the SCDs retrieved using 425–497 nm were the lowest. When we assume that the tropospheric b-AMF is nearly 1 in all the cases, the tropospheric $NO_2$ VCDs are comparable with the $NO_2$ SCDs; thus, the tropospheric $NO_2$ VCDs calculated in Beijing in winter were 3–6 times larger than those in the other cases depending on the fit windows and geometries. In the polluted region of interest, the standard deviations of the tropospheric $NO_2$ SCDs ranged from 0.19 to 0.27 $\times 10^{15}$ molec. $cm^{-2}$ (corresponding to 0.13–0.18 $\times 10^{15}$ molec. $cm^{-2}$ total $NO_2$ SCDs) in winter for all the fit windows, although in summer, they were as low as around 0.1 because higher SNRs were achieved. In winter, the $\varepsilon$ calculated using all the fit windows met our requirements (3.0%–3.8% at SNR = 920–1000), although none of the other cases showed results that met our requirements during summer. It should be noted that in the unpolluted region (Fig. 9), the $\varepsilon$ calculated using 425–497 nm increased, indicating that under clean and moderately polluted conditions, using the fit window of 425–497 nm would yield a lower $\varepsilon$.

### 3.1.2. Comparison between different satellite altitudes

Next, we compared the results calculated at different satellite altitudes (300 km and 600 km) to verify the feasibility of $NO_2$ detection from super-low satellite altitudes and conventional ones. In this comparison, we considered only the case of the Beijing area in winter as a representative to simplify the comparison. As shown in Fig. 10, the $\varepsilon$ values calculated using 300 km were 3.0% with SNR = 1000 (425–497 nm), 3.2% with SNR = 920 (405–465 nm), and 3.7% with SNR = 930 (425–450 nm), all of which met the scientific requirements. However, at a satellite altitude of 600 km, they did not meet the requirements because of lower SNRs < 500 ($\varepsilon$ = 6.0%–7.8%). The $\varepsilon$

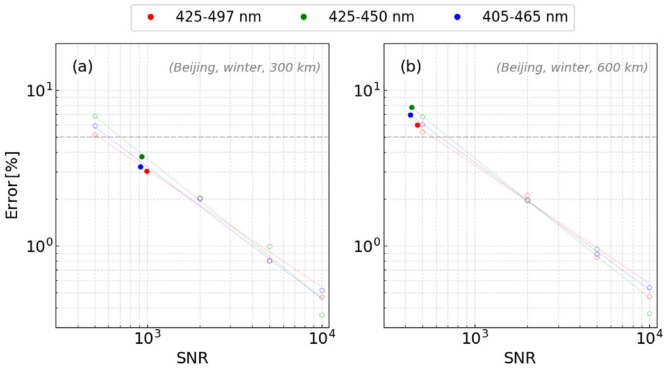


**Fig. 10.** Measurement errors of the tropospheric $NO_2$ SCDs (winter) calculated with albedo of 0.1 in Beijing at different satellite altitudes: (**a**) 300 km, (**b**) 600 km. The different colors represent the results of the different fit windows. (For interpretation of the references to color in this figure legend, the reader is referred to the Web version of this article.)

values at 300 km were two times larger than those at 600 km. It is obvious that a super-low satellite altitude of 300 km enables global observations with 1 × 1 $km^2$, which meets the scientific requirements.

### 3.1.3. Comparison between different surface albedo values

Similar to the comparison of different satellite altitudes, we compared the results calculated using different surface albedo values (0.05 and 0.1) by assuming a constant satellite altitude of 300 km and the vertical profile of Beijing in winter. As the surface albedo values in the observed area typically range from 0.04 to 0.08 annually as discussed above, it is reasonable to compare the values of 0.05 and 0.1 as typical values. Fig. 11 shows the relationship between $\varepsilon$ and the SNRs using the two albedo values of 0.05 and 0.1. The results with an albedo of 0.1 (circles) met the scientific requirements for all the fit windows, although the results with an albedo of 0.05 (triangles) did not meet the requirements except for the result using 425–497 nm. The $\varepsilon$ values with an albedo of 0.05 were 4.6% at SNR = 940 using 425–497 nm, 5.3% at

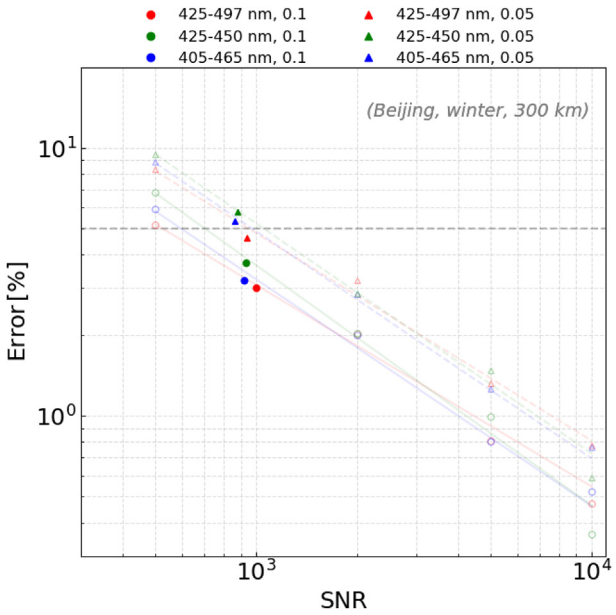


**Fig. 11.** Measurement errors of the tropospheric $NO_2$ SCDs (winter) calculated at a satellite altitude of 300 km in Beijing with different surface albedos of 0.05 (circle) and 0.1 (triangle). The different colors represent the different fit windows. Note that the y-axes in each panel have different scales. (For interpretation of the references to color in this figure legend, the reader is referred to the Web version of this article.)

SNR = 860 using 405–465 nm, and 5.8% at SNR = 880 using 425–450 nm.

#### 3.1.4. Overall comparison

In the discussion presented above, we individually compared the results calculated using different geometric parameters, profiles, and surface albedo values. Finally, we summarized each comparison and discussed the optimal setup of the fit window and satellite altitude. The calculated SNRs depended mainly on the assumed satellite altitudes owing to the dependency of the etendue, although they were comparable at the same altitude. The other factors related to the SNRs are the surface albedo and the fit windows, which caused the SNRs to vary within 10% for the same area and satellite altitude. The site dependence contributed the least to the SNRs, with a relative error of less than 5% in the same season, although the SNRs showed much higher dependency on the difference in season (approximately 25%), which indicates that the geometry in summer (smaller SZA) results in higher SNRs than that in winter (larger SZA).

In the highly polluted case, the results using a fit window of 425–497 nm showed the fewest measurement errors, whereas in most cases, use of the 425–450 nm window resulted in the highest uncertainty. In the polluted region, from a satellite altitude of 300 km during winter, all the cases achieved measurement errors of less than 5% with SNRs of around 1000. On the other hand, at a satellite altitude of 600 km, no case met the scientific requirements even in the polluted region. In the unpolluted region, the measurement errors were as high as 15%–55% for both altitudes, although it is not necessary to strictly adhere to the scientific requirements because this region is the control region. However, it is interesting that the $\varepsilon$ using 425–497 nm, which showed the lowest errors in the polluted region, resulted in high error values compared with the results derived from the other two fit windows, in spite of showing the best SNRs.

In summer, no results met the scientific requirements in the simulated cases. It should be noted that the results in summer showed fewer differences in the relative errors with regard to the fit windows than those in winter, implying that the choice of the fit window is more significant for $NO_2$ retrieval, especially in the polluted region and during winter, when the surface $NO_2$ tends to remain near the emission source.

Table 3 shows a summary of uncertainty estimates for each case calculated at a satellite altitude of 300 km. The relative differences in Beijing ranged from 3.0% to 13.3% largely depending on the season (i.e., profile shape) and fit window although those in Hokkaido ranged from 15.6% to 20.0% that were relatively high. On the basis of these results, we propose that the combination of a fit window of 425–497 nm and a satellite altitude of 300 km would be optimal for the proposed satellite instrument to achieve the scientific requirements when making observations in polluted regions. However, in the moderately polluted case, use of the 405–465 nm window resulted in fewer measurement errors than use of the 425–497 nm window, although it still did not satisfy the requirements. Therefore, the 405–465 nm fit window may be suitable when observing moderately polluted regions (around 3.0 × $10^{15}$ molec. $cm^{-2}$).

**Table 3**
Summary of uncertainty estimates for each case (satellite altitude of 300 km and surface albedo is fixed as 0.1 in winter and 0.05 in summer).

| Area | Season | Uncertainties [× $10^{15}$ molec. $cm^{-2}$] (%) | | |
|---|---|---|---|---|
| | | 425–450 nm | 425–497 nm | 405–465 nm |
| Beijing | Winter | 0.26 (3.7) | 0.19 (3.0) | 0.19 (3.2) |
| | Summer | 0.21 (8.9) | 0.14 (13.3) | 0.16 (8.8) |
| Hokkaido | Winter | 0.26 (16.5) | 0.18 (17.9) | 0.20 (15.6) |
| | Summer | 0.21 (18.7) | 0.15 (20.0) | 0.17 (17.6) |

### 3.2. Assessment of the sources of systematic error

The total error for the retrieved tropospheric VCD is determined by three main error sources: the measurement noise and systematic SCD errors, errors from the separation of the stratospheric and tropospheric $NO_2$, and errors from the uncertainties of the model parameters through the AMF calculation. The measurement noise is a source of random error. The systematic SCD errors include imperfect wavelength calibration, reference spectra errors, and spectral features of an instrument. These errors were negligible in this simulation on the basis of assumptions that the reference spectra used are true spectra and that there are no spectral features of an instrument. The errors from the separation of the stratospheric and tropospheric $NO_2$ depend on the uncertainties in the stratospheric $NO_2$ SCD, which is generally estimated to be of the order of 0.1–0.2 × $10^{15}$ molec. $cm^{-2}$ [64]. The errors from the AMF calculation consist of uncertainties in the model parameters, such as clouds, aerosols, and surface albedo, as well as the a priori $NO_2$ profile shape, which is estimated to be as large as up to 29% [48] on average in the region with large $NO_2$ emission sources, and it can have a considerable impact on the spatial distribution of $NO_2$ retrieved with kilometer-order resolution. Therefore, in practical retrieval of the tropospheric $NO_2$ VCD using a LEO satellite instrument, validation and model assimilation are required in subsequent analyses.

Boersma et al. [48] proposed an equation for the overall error variance of the tropospheric column owing to a satellite instrument considering error propagation. Based on this equation, the overall error for the tropospheric $NO_2$ retrieval was approximated as 0.88 × $10^{15}$ molec. $cm^{-2}$ under polluted conditions, assuming that the tropospheric AMF is 1 and that the error from the tropospheric AMF is 25%. This result is in good agreement with the scientific requirements assumed in this study.

## 4. Summary and conclusions

In this study, we determined the optimal fit window, satellite altitude, and sensor specification to meet the scientific requirements of measurement errors (5%) for tropospheric $NO_2$ observations using a small LEO satellite instrument with 1 × 1 $km^2$ horizontal resolution by simulating random instrumentation errors in the $NO_2$ SCDs. Specifically, we simulated backscattered radiance spectra in polluted and unpolluted regions (Beijing and Hokkaido, respectively) at two different satellite altitudes (300 km and 600 km) for two seasons (winter and summer), and we statistically analyzed the retrieved tropospheric $NO_2$ SCDs using the DOAS method to derive the relative SCD errors. As a result of the comprehensive analysis, the lower satellite altitude of 300 km was determined to be suitable to meet the scientific requirement of 5% for the tropospheric $NO_2$ SCD. The measurement error in the polluted region of interest (Beijing) met the scientific requirement of 5% at an SNR of around 1000 with a precision of 2%–4% for all the fit windows in the case of a satellite altitude of 300 km, while a satellite altitude of 600 km did not meet the requirements in the same situation. In the analysis for different surface albedo values (0.05 and 0.1), only a fit window of 425–497 nm met the scientific requirements (3% at SNR = 1000 with albedo = 0.1 and 4.6% at SNR = 940 with albedo = 0.05). In the moderately polluted case, use of the 405–465 nm window may be suitable because lower measurement errors are achieved compared to use of the 425–497 nm window, although it still did not satisfy the requirements. Therefore, a combination of a fit window of 425–497 nm and a satellite altitude of 300 km is likely to be the optimal combination for the satellite instrument considered in this study.

Table 4 summarizes the proposed sensor specifications compared to existing/potential satellite sensor specifications as well as the proposed spectrometer specification. The error estimation analysis considering the error propagation, including the AMF uncertainty, implied that the overall error for the tropospheric $NO_2$ retrieval was expected to be 0.88

**Table 4**
Summary of specifications for existing/future satellite instruments observing $NO_2$ within the UV/vis range and comparison with the proposed specification used in this study.

| Instrument (Platform) | Footprint | Satellite altitude | Spectral coverage | Spectral resolution | Uncertainty[i] |
|---|---|---|---|---|---|
| Unit | [km$^2$] | [km] | [nm] | [nm] | [molec cm$^{-2}$] |
| This study | 1 × 1 | 300 | 425–497 | 0.35 | 0.14 (0.19) × $10^{15}$ [a] |
| GOME (ERS-2) | 40 × 320 | 800 | 240–790 | 0.2–0.4 | 0.2–0.4 × $10^{15}$ [b] |
| SCIAMACHY (ENVISAT) | 30 × 60 | 800 | 214–812 | 0.2–0.5 | 1.4 × $10^{15}$ [c] |
| OMI (Aura) | 13 × 24 | 705 | 270–500 | 0.45–1.0 | 0.67 × $10^{15}$ [d] |
| GOME-2 (Metop-A,B,C) | 40 × 80 | 817 | 240–790 | 0.2–0.4 | 0.45 × $10^{15}$ [e] |
| TROPOMI (Sentinel-5P) | 3.5 × 7 | 824 | 270–495 | 0.25–0.55 | 0.7 × $10^{15}$ [f] |
| Spectrolite | 1 km [g] | 600 | 320–495 | < 0.5 | < 3 × $10^{15}$ [h] |

[a] Uncertainties of total (tropospheric) $NO_2$ SCDs estimated in this study.
[b] Richter and Burrows [7]. Boersma et al. [48] reported 0.55 × $10^{15}$ molec. cm$^{-2}$.
[c] Richter et al. [56].
[d] Boersma et al. [65].
[e] Valks et al. [66]. Richter et al. [56] also reported 1.2 × $10^{15}$ molec cm$^{-2}$ but using 425–497 nm instead of 425–450 nm.
[f] van Geffen et al. [67].
[g] On across track. IFOV = 0.1°.
[h] de Goeij et al. [22].
[i] Random errors of total slant columns.

× $10^{15}$ molec. cm$^{-2}$, which is consistent with the scientific requirements. As shown in Table 4, the satellite instrument proposed in this study showed lower uncertainties of the retrieved total and tropospheric $NO_2$ SCDs without deterioration of the spectral resolution, compared with those of the other satellite instruments. This can be achieved using an extremely low satellite altitude of 300 km. In addition, we proposed the spectrometer specification optimized for $NO_2$ observation with a resolution of 1 × 1 km$^2$ and an F number of 2.6–5.3, leading to high SNRs as well as good measurement precision. These results have demonstrated the feasibility of the proposed spectrometer design, which will not only achieve a sufficiently high spatial resolution to identify and separate urban sources of $NO_2$ but also facilitate the determination of their emissions.

## Acknowledgements

We are deeply grateful to Vladimir and Alexei Rozanov of IUP/University of Bremen for providing access to the SCIATRAN model. We would like to thank Kazuyuki Miyazaki of JAMSTEC for providing results of the CHASER model simulation.

## Appendix A

Table A.1
Aerosol scenarios for each region and season.

| Area | Layer Num. | Altitude range | Aerosol types | Components and number mixing ratio | Relative humidity |
|---|---|---|---|---|---|
| Beijing | #1 | 0–2 km | Urban | Water soluble: 0.177 insoluble:0.949E-5 soot:0.823 | Winter: 50% Summer: 70% |
| | #2 | 2–10 km | Continental average | Water soluble: 0.458 insoluble:0.261E-4 soot:0.542 | Winter: 50% Summer: 70% |
| | #3 | 10–30 km | Sulfate | sulfate: 1 | 0% |
| | #4 | 30–100 km | Meteoric | meteoric dust: 1 | 0% |
| Hokkaido | #1 | 0–2 km | Continental average | Water soluble: 0.458 insoluble:0.261E-4 soot:0.542 | Winter: 70% Summer: 80% |
| | #2 | 2–10 km | Continental average | Water soluble: 0.458 insoluble:0.261E-4 soot:0.542 | Winter: 70% Summer: 80% |
| | #3 | 10–30 km | Sulfate | sulfate: 1 | 0% |
| | #4 | 30–100 km | Meteoric | meteoric dust: 1 | 0% |

## References

[1] World Health Organization, Ambient (Outdoor) Air Quality and Health, (2016) http://www.who.int/mediacentre/factsheets/fs313/en/.
[2] S. Beirle, K.F. Boersma, U. Platt, M.G. Lawrence, T. Wagner, Megacity emissions and lifetimes of nitrogen oxides probed from space, Science 333 (6050) (2011) 1737–1739, https://doi.org/10.1126/science.1207824.
[3] J.P. Burrows, M. Weber, M. Buchwitz, V. Rozanov, A. Ladstätter-Weißenmayer, A. Richter, R. DeBeek, R. Hoogen, K. Bramstedt, K.-U. Eichmann, M. Eisinger, D. Perner, J.P. Burrows, M. Weber, M. Buchwitz, V. Rozanov, A. Ladstätter-Weißenmayer, A. Richter, R. DeBeek, R. Hoogen, K. Bramstedt, K.-U. Eichmann, M. Eisinger, D. Perner, The global ozone monitoring experiment (GOME): mission concept and first scientific results, J. Atmos. Sci. 56 (2) (1999) 151–175, https://doi.org/10.1175/1520-0469(1999)056<0151:TGOMEG>2.0.CO;2.
[4] H. Bovensmann, J.P. Burrows, M. Buchwitz, J. Frerick, S. Noël, V.V. Rozanov, K.V. Chance, A.P.H. Goede, SCIAMACHY: mission objectives and measurement modes, J. Atmos. Sci. 56 (2) (1999) 127–150, https://doi.org/10.1175/1520-0469(1999)056<0127:SMOAMM>2.0.CO;2.
[5] P.F. Levelt, G.H.J. van den Oord, M.R. Dobber, A. Malkki, H. Visser, J. de Vries,

P. Stammes, J.O.V. Lundell, H. Saari, The ozone monitoring instrument, IEEE Trans. Geosci. Remote Sens. 44 (5) (2006) 1093–1101, https://doi.org/10.1109/TGRS.2006.872333.
[6] J. Callies, E. Corpaccioli, M. Eisinger, A. Hahne, A. Lefebvre, GOME-2 - metop's second-generation sensor for operational ozone monitoring, ESA Bull. Space Agency 102 (2000) 28–36.
[7] A. Richter, J. Burrows, Tropospheric $NO_2$ from GOME measurements, Adv. Space Res. 29 (11) (2002) 1673–1683, https://doi.org/10.1016/S0273-1177(0200100-X).
[8] S. Beirle, U. Platt, M. Wenig, T. Wagner, Atmospheric Chemistry and Physics Weekly cycle of $NO^2$ by GOME measurements: a signature of anthropogenic sources, Atmos. Chem. Phys. 3 (2003) 2225–2232.
[9] A. Richter, J.P. Burrows, H. Nüß, C. Granier, U. Niemeier, Increase in tropospheric nitrogen dioxide over China observed from space, Nature 437 (7055) (2005) 129–132, https://doi.org/10.1038/nature04092.
[10] S.-W. Kim, A. Heckel, S.A. McKeen, G.J. Frost, E.-Y. Hsie, M.K. Trainer, A. Richter, J.P. Burrows, S.E. Peckham, G.A. Grell, Satellite-observed U.S. power plant $NO_x$ emission reductions and their impact on air quality, Geophys. Res. Lett. 33 (22) (2006) L22812, https://doi.org/10.1029/2006GL027749.
[11] R.J. van der A, D.H. Peters, H. Eskes, K.F. Boersma, M. Van Roozendael, I. De Smedt, H.M. Kelder, Detection of the trend and seasonal variation in tropospheric $NO^2$ over China, J. Geophys. Res. Atmos 111 (12) (2006) 1–10, https://doi.org/10.1029/2005JD006594.
[12] R.J. van der A, H.J. Eskes, K.F. Boersma, T.P. van Noije, M. Van Roozendael, I. De Smedt, D.H. Peters, E.W. Meijer, Trends, seasonal variability and dominant $NO_x$ source derived from a ten year record of $NO^2$ measured from space, J. Geophys. Res. Atmos 113 (4) (2008) D04302, https://doi.org/10.1029/2007JD009021.
[13] T. Stavrakou, J.-F. Müller, K.F. Boersma, I. De Smedt, R.J. van der A, Assessing the distribution and growth rates of $NO_x$ emission sources by inverting a 10-year record of $NO_2$ satellite columns, Geophys. Res. Lett. 35 (10) (2008) L10801, https://doi.org/10.1029/2008GL033521.
[14] K.F. Boersma, H.J. Eskes, R.J. Dirksen, R.J. Van Der A, J.P. Veefkind, P. Stammes, V. Huijnen, Q.L. Kleipool, M. Sneep, J. Claas, J. Leitão, A. Richter, Y. Zhou, D. Brunner, An improved tropospheric $NO^2$ column retrieval algorithm for the Ozone Monitoring Instrument, Atmos. Meas. Tech 4 (9) (2011) 1905–1928, https://doi.org/10.5194/amt-4-1905-2011.
[15] L.N. Lamsal, R.V. Martin, A. Padmanabhan, A. van Donkelaar, Q. Zhang, C.E. Sioris, K. Chance, T.P. Kurosu, M.J. Newchurch, Application of satellite observations for timely updates to global anthropogenic $NO_x$ emission inventories, Geophys. Res. Lett. 38 (5) (2011) L05810, https://doi.org/10.1029/2010GL046476.
[16] A. Hilboll, A. Richter, J.P. Burrows, Long-term changes of tropospheric $NO^2$ over megacities derived from multiple satellite instruments, Atmos. Chem. Phys. 13 (8) (2013) 4145–4169, https://doi.org/10.5194/acp-13-4145-2013.
[17] B.N. Duncan, L.N. Lamsal, A.M. Thompson, Y. Yoshida, Z. Lu, D.G. Streets, M.M. Hurwitz, K.E. Pickering, A space-based, high-resolution view of notable changes in urban $NO_x$ pollution around the world (20052014), J. Geophys. Res. 121 (2) (2016) 976–996, https://doi.org/10.1002/2015JD024121.
[18] P. Ingmann, B. Veihelmann, J. Langen, D. Lamarre, H. Stark, G.B. Courrèges-Lacoste, Requirements for the GMES atmosphere service and ESA's implementation concept: sentinels-4/-5 and -5p, Remote Sens. Environ. 120 (2012) 58–69, https://doi.org/10.1016/j.rse.2012.01.023.
[19] L. Flynn, J. Hornstein, E. Hilsenrath, The ozone mapping and profiler suite (OMPS). The next generation of US ozone monitoring instruments, Geosci. Remote Sens. Symp. 2004. IGARSS '04. Proceedings. 2004 IEEE Int. 1 (C), 2004, pp. 152–155, , https://doi.org/10.1109/IGARSS.2004.1368968.
[20] J. Kim, GEMS (geostationary environment monitoring spectrometer) onboard the GeoKOMPSAT to monitor air quality in high temporal and spatial resolution over asia-pacific region, EGU Gene Assem. (2012) held 22-27 April. 2012 Vienna, Austria., p.4051 14 (2012) 4051.
[21] P. Zoogman, X. Liu, R.M. Suleiman, W.F. Pennington, D.E. Flittner, J.A. Al-Saadi, B.B. Hilton, D.K. Nicks, M.J. Newchurch, J.L. Carr, S.J. Janz, M.R. Andraschko, A. Arola, B.D. Baker, B.P. Canova, C. Chan Miller, R.C. Cohen, J.E. Davis, M.E. Dussault, D.P. Edwards, J. Fishman, A. Ghulam, G. González Abad, M. Grutter, J.R. Herman, J. Houck, D.J. Jacob, J. Joiner, B.J. Kerridge, J. Kim, N.A. Krotkov, L. Lamsal, C. Li, A. Lindfors, R.V. Martin, C.T. McElroy, C. McLinden, V. Natraj, D.O. Neil, C.R. Nowlan, E.J. O'Sullivan, P.I. Palmer, R.B. Pierce, M.R. Pippin, A. Saiz-Lopez, R.J. Spurr, J.J. Szykman, O. Torres, J.P. Veefkind, B. Veihelmann, H. Wang, J. Wang, K. Chance, Tropospheric emissions: monitoring of pollution (TEMPO), J. Quant. Spectrosc. Radiat. Transf. 186 (2017) 17–39, https://doi.org/10.1016/j.jqsrt.2016.05.008.
[22] B.T.G. de Goeij, J.M.O. van Wakeren, J.P. Veefkind, T. Vlemmix, X. Ge, B.P.F. Dirks, P.M. Toet, L.F. van der Wal, R. Jansen, G.C.J. Otter, P.F. Levelt, First aircraft test results of a compact, low cost hyperspectral imager for earth observation from space, in: N. Karafolas, B. Cugny, Z. Sodnik (Eds.), Int. Conf. Sp. Opt. ICSO 2016, vol. 10562, SPIE, 2017, p. 41, , https://doi.org/10.1117/12.2296068.
[23] Y. Wang, J. Lampel, P. Xie, S. Beirle, A. Li, D. Wu, T. Wagner, Ground-based MAX-DOAS observations of tropospheric aerosols, $NO^2$, $SO^2$ and HCHO in Wuxi, China, from 2011 to 2014, Atmos. Chem. Phys. 17 (2017) 2189–2215, https://doi.org/10.5194/acp-17-2189-2017.
[24] Q. Hong, C. Liu, K.L. Chan, Q. Hu, Z. Xie, H. Liu, F. Si, J. Liu, Ship-based MAX-DOAS measurements of tropospheric $NO^2$, $SO^2$, and HCHO distribution along the Yangtze River, Atmos. Chem. Phys. 18 (8) (2018) 5931–5951, https://doi.org/10.5194/acp-18-5931-2018.
[25] A.C. Meier, A. Schönhardt, T. Bösch, A. Richter, A. Seyler, T. Ruhtz, D.E. Constantin, R. Shaiganfar, T. Wagner, A. Merlaud, M.V. Roozendael, L. Belegante, D. Nicolae, L. Georgescu, J.P. Burrows, High-resolution airborne imaging DOAS measurements of $NO^2$ above Bucharest during AROMAT, Atmos. Meas. Tech 10 (5) (2017) 1831–1857, https://doi.org/10.5194/amt-10-1831-2017.
[26] H. Akimoto, Y. Kasai, K. Kita, H. Irie, K. Sagi, S. Hayashida, Geostationary atmospheric observation satellite plan in Japan, AGU Fall Meet. Abstr. 2009.
[27] Y. Kasai, K. Kita, Y. Kanaya, A.M. Team, Others, the Japanese air pollusion observation missions, GMAP-asia and APOLLO, AGU Fall Meet. Abstr. 2011.
[28] A. Schönhardt, P. Altube, K. Gerilowski, S. Krautwurst, J. Hartmann, A.C. Meier, A. Richter, J.P. Burrows, A wide field-of-view imaging DOAS instrument for two-dimensional trace gas mapping from aircraft, Atmos. Meas. Tech. 8 (12) (2015) 5113–5131, https://doi.org/10.5194/amt-8-5113-2015.
[29] A. Seyler, A.C. Meier, F. Wittrock, L. Kattner, B. Mathieu-Üffing, E. Peters, A. Richter, T. Ruhtz, A. Schönhardt, S. Schmolke, J.P. Burrows, Studies of the horizontal inhomogeneities in $NO^2$; concentrations above a shipping lane using ground-based MAX-DOAS and airborne imaging DOAS measurements, Atmos. Meas. Tech. Discuss. 2 (2018) 1–26, https://doi.org/10.5194/amt-2018-348.
[30] A. Merlaud, F. Tack, D.-E. Constantin, L. Georgescu, J. Maes, C. Fayt, F. Mingireanu, D. Schuettemeyer, A.C. Meier, A. Schönardt, T. Ruhtz, L. Bellegante, D. Nicolae, M. Den Hoed, M. Allaart, M. Van Roozendael, The Small Whiskbroom Imager for atmospheric compositioN monitorinG (SWING) and its operations from an unmanned aerial vehicle (UAV) during the AROMAT campaign, Atmos. Meas. Tech. 11 (1) (2018) 551–567, https://doi.org/10.5194/amt-11-551-2018.
[31] F. Tack, A. Merlaud, A.C. Meier, T. Vlemmix, T. Ruhtz, M.-D. Iordache, X. Ge, L. van der Wal, D. Schuettemeyer, M. Ardelean, A. Calcan, A. Schönhardt, K. Meuleman, A. Richter, M. Van Roozendael, Intercomparison of four airborne imaging DOAS systems for tropospheric $NO^2$; mapping – the AROMAPEX campaign, Atmos. Meas. Tech. Discuss. 2 (2018) 1–48, https://doi.org/10.5194/amt-2017-478.
[32] A.C. Meier, Measurements of Horizontal Trace Gas Distributions Using Airborne Imaging Differential Optical Absorption Spectroscopy, PhD dissertation University of Bremen, 2018.
[33] H. Nagano, K. Kajiwara, H. Osuga, T. Ozaki, T. Nakagawa, Research and development of a new power processing control unit of ion engine system for the super low altitude test satellite, Trans. Japan Soc. Aeronaut. Space Sci. Aerosp. Technol. Jpn 8 (ists27) (2010), https://doi.org/10.2322/tastj.8.Tb_17 Tb_17–Tb_22.
[34] H. Kawasaki, K. Konoue, H. Hoshino, Y. Kaneko, M. Sasaki, Interim report of super low altitude satellite operation, IGARSS 2018 - 2018 IEEE Int. Geosci. Remote Sens. Symp., IEEE, 2018, pp. 4066–4069, , https://doi.org/10.1109/IGARSS.2018.8517529 https://ieeexplore.ieee.org/document/8517529/.
[35] A. Rozanov, V. Rozanov, M. Buchwitz, A. Kokhanovsky, J.P. Burrows, SCIATRAN 2.0 - a new radiative transfer model for geophysical applications in the 175-2400 nm spectral region, Adv. Space Res. 36 (5) (2005) 1015–1019, https://doi.org/10.1016/j.asr.2005.03.012.
[36] H. Irie, H. Iwabuchi, Y. Kasai, K. Kita, H. Akimoto, A simulation for UV-VIS observations of tropospheric composition from a GEO satellite over Asia, AGU Fall Meet. Abstr. 2009.
[37] H. Irie, H. Iwabuchi, K. Noguchi, Y. Kasai, K. Kita, H. Akimoto, Quantifying the relationship between the measurement precision and specifications of a UV/visible sensor on a geostationary satellite, Adv. Space Res. 49 (12) (2012) 1743–1749, https://doi.org/10.1016/j.asr.2012.03.012 https://doi.org/10.1016/j.asr.2012.03.012.
[38] K. Noguchi, A. Richter, H. Bovensmann, A. Hilboll, J.P. Burrows, H. Irie, S. Hayashida, Y. Morino, A feasibility study for the detection of the diurnal variation of tropospheric $NO^2$ over Tokyo from a geostationary orbit, Adv. Space Res. 48 (9) (2011) 1551–1564, https://doi.org/10.1016/j.asr.2011.06.029.
[39] J.Z. Ma, S. Beirle, J.L. Jin, R. Shaiganfar, P. Yan, T. Wagner, Tropospheric $NO^2$ vertical column densities over Beijing: results of the first three years of ground-based MAX-DOAS measurements (2008-2011) and satellite validation, Atmos. Chem. Phys. 13 (3) (2013) 1547–1567, https://doi.org/10.5194/acp-13-1547-2013.
[40] F. Hendrick, K. Clémer, P. Wang, M. De Mazière, C. Fayt, C. Gielen, C. Hermans, J.Z. Ma, G. Pinardi, T. Stavrakou, T. Vlemmix, M. Van Roozendael, Four years of ground-based MAX-DOAS observations of HONO and $NO^2$ in the Beijing area, Atmos. Chem. Phys. 14 (2) (2014) 765–781, https://doi.org/10.5194/acp-14-765-2014.
[41] Y. Kanaya, H. Irie, H. Takashima, H. Iwabuchi, H. Akimoto, K. Sudo, M. Gu, J. Chong, Y.J. Kim, H. Lee, A. Li, F. Si, J. Xu, P.-H. Xie, W.-Q. Liu, A. Dzhola, O. Postylyakov, V. Ivanov, E. Grechko, S. Terpugova, M. Panchenko, Long-term MAX-DOAS network observations of $NO^2$ in Russia and Asia (MADRAS) during the period 20072012: instrumentation, elucidation of climatology, and comparisons with OMI satellite observations and global model simulations, Atmos. Chem. Phys. 14 (2014) 7909–7927, https://doi.org/10.5194/acp-14-7909-2014.
[42] K. Chance, R.L. Kurucz, An improved high-resolution solar reference spectrum for earth's atmosphere measurements in the ultraviolet, visible, and near infrared, J. Quant. Spectrosc. Radiat. Transf. 111 (9) (2010) 1289–1295, https://doi.org/10.1016/j.jqsrt.2010.01.036.
[43] K. Sudo, M. Takahashi, J.I. Kurokawa, H. Akimoto, CHASER: a global chemical model of the troposphere 1. Model description, J. Geophys. Res. Atmos. 107 (17) (2002), https://doi.org/10.1029/2001JD001113.
[44] S. Itahashi, I. Uno, H. Irie, J.I. Kurokawa, T. Ohara, Regional modeling of tropospheric $NO^2$ vertical column density over East Asia during the period 2000-2010: comparison with multisatellite observations, Atmos. Chem. Phys. 14 (7) (2014) 3623–3635, https://doi.org/10.5194/acp-14-3623-2014.
[45] K. Sudo, M. Takahashi, H. Akimoto, CHASER: a global chemical model of the troposphere 2. Model results and evaluation, J. Geophys. Res. Atmos. 107 (D21) (2002), https://doi.org/10.1029/2001JD001114 ACH 9–1–ACH 9–39.
[46] G. Brasseur, S. Walters, M.H. Hitchman, M. Dymek, E. Falise, An interactive chemical dynamical radiative two-dimensional model of the middle atmosphere, J.

Geophys. Res. 95 (D5) (1990) 5639–5655, https://doi.org/10.1029/JD095iD05p05639.
[47] Q. Kleipool, OMI/Aura Surface Reflectance Climatology L3 Global Gridded 0.5 Degree X 0.5 Degree V3, Greenbelt, MD, USA, Goddard Earth Sciences Data and Information Services Center (GES DISC), 2010, https://doi.org/10.5067/Aura/OMI/DATA3006 , Accessed date: 19 October 2018.
[48] K.F. Boersma, H.J. Eskes, E.J. Brinksma, Error analysis for tropospheric $NO^2$ retrieval from space, J. Geophys. Res. Atmos 109 (D4) (2004) D04311, https://doi.org/10.1029/2003JD003962.
[49] M. Hess, P. Koepke, I. Schult, Optical properties of aerosols and clouds, Bull. Am. Meteorol. Soc. 79 (1998) 831–844, https://doi.org/10.1175/1520-0477(1998)079<0831:OPOAAC>2.0.CO;2.
[50] A. Kuze, T. Imai, H. Suto, 1-km resolution mapping from space with a sub-nanometer spectral resolution imaging spectrometer, Hyperspectral Imaging Sound. Environ. HISE 2015, OSA, Washington, D.C., 2015, p. HM4B.2, , https://doi.org/10.1364/HISE.2015.HM4B.2.
[51] A. Kuze, H. Suto, Imaging spectrometer with an agile pointing system to quantify global and regional greenhouse gas fluxes and monitor localized emission sources, Trans. JSASS Aero. Tech. Jpn 16 (2) (2018) 147–151, https://doi.org/10.2322/tastj.16.147.
[52] K. Noguchi, A. Richter, V. Rozanov, A. Rozanov, J.P. Burrows, H. Irie, K. Kita, Effect of surface BRDF of various land cover types on geostationary observations of tropospheric $NO^2$, Atmos. Meas. Tech 7 (10) (2014) 3497–3508, https://doi.org/10.5194/amt-7-3497-2014.
[53] U. Platt, Differential optical absorption spectroscopy (DOAS), in: M.W. Sigrist (Ed.), Air Monitoring by Spectroscopic Techniques, 1994, pp. 27–84 Chem. Anal. Ser. 127.
[54] J.F. Grainger, J. Ring, Anomalous fraunhofer line profiles, Nature 193 (4817) (1962), https://doi.org/10.1038/193762a0 762–762.
[55] E. Bucsela, E. Celarier, M. Wenig, J. Gleason, J. Veefkind, K. Boersma, E. Brinksma, Algorithm for $NO^2$ vertical column retrieval from the ozone monitoring instrument, IEEE Trans. Geosci. Remote Sens. 44 (5) (2006) 1245–1258, https://doi.org/10.1109/TGRS.2005.863715.
[56] A. Richter, M. Begoin, A. Hilboll, J.P. Burrows, An improved $NO^2$ retrieval for the GOME-2 satellite instrument, Atmos. Meas. Tech 4 (6) (2011) 1147–1159, https://doi.org/10.5194/amt-4-1147-2011.
[57] A.C. Vandaele, C. Hermans, S. Fally, M. Carleer, R. Colin, M. Merienne, A. Jenouvrier, B. Coquart, High-resolution Fourier transform measurement of the NO 2 visible and near-infrared absorption cross sections: temperature and pressure effects, J. Geophys. Res. 107 (D18) (2002) 4348, https://doi.org/10.1029/2001JD000971 https://agupubs.onlinelibrary.wiley.com/doi/full/10.1029/2001JD000971Ωhttp://doi.wiley.com/10.1029/2001JD000971.
[58] A. Serdyuchenko, V. Gorshelev, M. Weber, W. Chehade, J.P. Burrows, High spectral resolution ozone absorption cross-sections Part 2: temperature dependence, Atmos. Meas. Tech 7 (2014) 625–636, https://doi.org/10.5194/amt-7-625-2014 www.atmos-meas-tech.net/7/625/2014/.
[59] R. Thalman, R. Volkamer, Temperature dependent absorption cross-sections of O2O2 collision pairs between 340 and 630 nm and at atmospherically relevant pressure, Phys. Chem. Chem. Phys. 15 (37) (2013) 15371, https://doi.org/10.1039/c3cp50968k https://www.colorado.edu/chemistry/volkamer/publications/articles/T-and-V-2013-O4-PCCPaccepted.pdfΩhttp://xlink.rsc.org/?DOI=c3cp50968k.
[60] L.S. Rothman, I.E. Gordon, A. Barbe, D.C. Benner, P.F. Bernath, M. Birk, V. Boudon, L.R. Brown, A. Campargue, J.P. Champion, K. Chance, L.H. Coudert, V. Dana, V.M. Devi, S. Fally, J.M. Flaud, R.R. Gamache, A. Goldman, D. Jacquemart, I. Kleiner, N. Lacome, W.J. Lafferty, J.Y. Mandin, S.T. Massie, S.N. Mikhailenko, C.E. Miller, N. Moazzen-Ahmadi, O.V. Naumenko, A.V. Nikitin, J. Orphal, V.I. Perevalov, A. Perrin, A. Predoi-Cross, C.P. Rinsland, M. Rotger, M. Šimečková, M.A. Smith, K. Sung, S.A. Tashkun, J. Tennyson, R.A. Toth, A.C. Vandaele, J. Vander Auwera, The HITRAN 2008 molecular spectroscopic database, J. Quant. Spectrosc. Radiat. Transf. 110 (9–10) (2009) 533–572, https://doi.org/10.1016/j.jqsrt.2009.02.013.
[61] M. Vountas, V.V. Rozanov, J.P. Burrows, Ring effect: impact of rotational Raman scattering on radiative transfer in earth's atmosphere, J. Quant. Spectrosc. Radiat. Transf. 60 (6) (1998) 943–961, https://doi.org/10.1016/S0022-4073(97)00186-6.
[62] G.J.M. Velders, C. Granier, R.W. Portmann, K. Pfeilsticker, M. Wenig, T. Wagner, U. Platt, A. Richter, J.P. Burrows, Global tropospheric $NO^2$ column distributions: comparing three-dimensional model calculations with GOME measurements, J. Geophys. Res. Atmos 106 (D12) (2001) 12643–12660, https://doi.org/10.1029/2000JD900762.
[63] R.V. Martin, K. Chance, D.J. Jacob, T.P. Kurosu, R.J. Spurr, E. Bucsela, J.F. Gleason, P.I. Palmer, I. Bey, A.M. Fiore, Q. Li, R.M. Yantosca, R.B. Koelemeijer, An improved retrieval of tropospheric nitrogen dioxide from GOME, J. Geophys. Res. D Atmos. 107 (2002), https://doi.org/10.1029/2001JD001027.
[64] R.J. Dirksen, K.F. Boersma, H.J. Eskes, D.V. Ionov, E.J. Bucsela, P.F. Levelt, H.M. Kelder, Evaluation of stratospheric $NO^2$ retrieved from the Ozone Monitoring Instrument: intercomparison, diurnal cycle, and trending, J. Geophys. Res. Atmos 116 (8) (2011) 1–22, https://doi.org/10.1029/2010JD014943.
[65] K.F. Boersma, H.J. Eskes, J.P. Veefkind, E.J. Brinksma, R. J. V. D. A, M. Sneep, G.H.J.V. den Oord, P.F. Levelt, P. Stammes, J.F. Gleason, E.J. Bucsela, Near-real time retrieval of tropospheric $NO^2$ from OMI, Atmos. Chem. Phys. 7 (8) (2007) 2103–2118.
[66] P. Valks, G. Pinardi, A. Richter, J.C. Lambert, N. Hao, D. Loyola, M. Van Roozendael, S. Emmadi, Operational total and tropospheric $NO^2$ column retrieval for GOME–2, Atmos. Meas. Tech 4 (7) (2011) 1491–1514, https://doi.org/10.5194/amt-4-1491-2011.
[67] J.H.G.M. van Geffen, H.J. Eskes, K.F. Boersma, J.D. Maasakkers, J.P. Veefkind, TROPOMI ATBD of the total and tropospheric NO$_2$ data products, Tech. Rep. (2014), http://www.tropomi.eu/documents/atbd , Accessed date: 30 October 2018.